![White Rose university consortium logo — Universities of Leeds, Sheffield & York]

Measurement and density normalisation of acoustic attenuation and backscattering constants of arbitrary suspensions within the Rayleigh scattering regime

Jaiyana Bux[a], Jeff Peakall[b], Hugh P. Rice[a], Mohamed S. Manga[a], Simon Biggs[c], Timothy N. Hunter[a]*

[a] School of Chemical and Process Engineering, University of Leeds, Leeds, LS2 9JT, UK

[b] School of Earth and Environment, University of Leeds, Leeds, LS2 9JT, UK

[c] School of Chemical Engineering, The University of Queensland, Brisbane, Queensland 4072, Australia

*Corresponding author: email; t.n.hunter@leeds.ac.uk

Draft Submission: 23 Jan 2018

Date of Acceptance: 20 Oct 2018

ABSTRACT

The scattering and attenuation of megahertz frequency acoustic backscatter in liquid suspensions, is examined for a range of fine organic and inorganic particles in the Rayleigh regime, $10^{-4} <$ ka $< 10^{0}$ (where k is the wavenumber and a the particle radius) which are widely industrially relevant, but with limited existing data. In particular, colloidal latex, mineral titania and barytes sediments, as well as larger glass powders were investigated. A manipulation of the backscatter voltage equation was used to directly measure the sediment attenuation constants, ξ. Decoupling of the combined backscattering-transducer constant, allowing explicit measurement of the backscattering constant, k_s, was achieved through calibration of the transducer constant, k_t. Additionally, the methodology was streamlined via averaging between a number of intermediate concentrations to reduce data variability. This approach enabled the form function, f, and the corresponding total normalized scattering cross-sections, χ, to be determined for all species. While f and χ are available in the literature for large glass and sand, this methodology allowed extension for the colloidal organic and inorganic particles. Specific gravity normalisation of f collapsed all data onto a single distribution, with the exception of titania, due to scattering complexities associated with agglomeration. There was some additional variation in χ, with measured values of the fine particles up to of magnitude greater than the density-normalised prediction at low ka. Mechanisms accounting for these variations from theory are however analysed, and include viscous attenuation effects, the polydispersity of the particle type and increasing influence of the solvent attenuation. Additionally, thermoacoustic losses appeared to dominate the attenuation behaviour of the organic latex particles. This study demonstrates that particles close to the colloidal regime can be measured successfully with acoustic backscatter, and highlights the great potential of this technique to be applied for in situ or online monitoring purposes in such systems.

1   Introduction

Acoustic backscatter systems show significant potential for the measurement of solids concentration and size in many suspensions, in both environmental and engineering fields. The primary advantage of ultrasound, is the improved depth penetration in concentrated and opaque media, compared with optical based methods, such as laser scattering [1], CCD video techniques [2] and optical backscatter systems [3]. In situ backscatter devices, which measure the echo

response, also offer better application flexibility than instrumentation which incorporate separate transmitters and receivers, including electrical tomographic methods [4, 5], gamma or x-ray densitometers [6, 7], as well as ultrasonic transmission methods [8-11]. Both single-frequency and array-based echo techniques are now widely utilised to measure particle properties in relatively low-concentration environmental sediment transport studies [12-15], and similar methods are being investigated for a number of industrial fields [16-22].

A key challenge with utilising the theoretical approaches in solving backscatter voltage equations (to extract particle size and concentration information) is the requirement to define the backscattering constant (k_s) and the sediment attenuation coefficient (ξ) for the particle system of interest. These parameters are derived from correlations of the dimensionless form function, f, and total normalised scattering cross-section, χ, respectively. Such correlations exist for large non-cohesive particles; glass beads and sandy sediments [15, 23, 24]; however, data are not currently available for organic particles and many minerals, which are of interest in engineering systems. Furthermore, existing data are limited with respect to small grain sizes, especially within the Rayleigh scattering regime ($ka < 1$, where k is the wavenumber and a the particle radius).

Rice and co-workers [25] have previously outlined a method for measuring the attenuation constants of particles in suspension. It utilised the Thorne and Hanes [15] model for dilute marine sediment applications, which is based on parameterising the return echo voltage to various particle properties, specifically size and concentration. The method facilitated the characterisation of suspensions comprising arbitrary particle types, although it was limited by an inability to separate the backscattering constant of the particles, k_s, from the influence of the transducer constant, k_t. The current authors have previously undertaken similar analysis alongside phenomenological approaches to characterise concentrated, settling and turbulent dispersions of large glass beads, plastic particles and colloidal minerals in pipe flows, as well as small and large industrial scale tanks [26-32]. Collectively, this research provides pathways to enable online characterisation of many concentrated dispersion systems in industries ranging from cosmetic, pharmaceutical, food and paint products, to water treatment, minerals and nuclear waste processing. However, due to a lack of specific information on the backscatter coefficients of these engineering suspensions, quantitative assessment using established theory was restricted.

To help overcome the current lack of engineering data and theoretical limitations, this paper presents a rapid, phenomenological approach for determining these acoustic parameters for a number of fine sediments with varying densities, of general relevance to process engineering systems. While the method outlined by Rice and co-workers [25] has previously been utilised to independently measure the attenuation constant, it will be extended by calibrating the transducers to enable quantification of k_s for arbitrary particle types. Specifically, we initially examine the values of k_s for spherical glass particles, where the scattering attenuation is dominant, due to the large scattering cross-section resulting in acoustic losses at angles other than 180° [33]. Acoustic responses will also be compared to fine inorganic minerals; barium sulphate and titanium dioxide, which predominantly incur viscous losses due to small grain size and large density contrast between the particles and dispersant [34]. Colloidal organic emulsions and latex dispersions will additionally be measured, where the thermoacoustic scattering effects are dominant from the minimal density contrast between the particles and fluid [34]. Normalised f and χ functions are subsequently determined for the first time for these systems, from directly measured values of ξ and k_s.

Colloidal particle systems have historically been characterised via ex situ broadband ultrasonic spectroscopic devices, with separate transmitting and receiving transducers, comprising measurement depths of only a few centimetres [9-11]. Measurement of these particle types with larger-scale profilers is challenging, as the reduced backscatter intensity from colloidal grain sizes and high levels of acoustic attenuation incurred from thermal losses, which may introduce instrument limitations. Collectively, these dispersions provide acoustical responses within the Rayleigh scattering range, $10^{-4} < ka < 10^0$, where data are currently limited. Hence, they will facilitate the assessment of the backscattering and attenuating behaviour of particles with small grain sizes and a range of acoustic properties. This final outcome will assist in closing the knowledge gap for small particles, which are important in suspension applications in engineering, as well as improving understanding of the acoustic response of individual particulates and aggregates within large floc structures.

2   Theory and calibration procedure

The acoustic backscattering theoretical approach is summarised in a review by Thorne and Hanes [15], which is extensively used by marine scientists for particle size and concentration measurements, especially in dilute environments (< 1 g/L) comprising large sediment grain sizes (radii > 40 µm) [35]. The model is described in the Appendix (see Eq. A.1-A.9) and requires knowledge of the sediment's backscattering and attenuating properties. Specifically, the backscattering constant k_s is derived from the dimensionless form function, f, which describes the sediment's backscattering properties as a function of its size and the insonifying frequency. The sediment attenuation coefficient, ξ, is derived from the dimensionless total normalised scattering cross-section, χ, which quantifies the sediment's attenuating properties due to scattering and absorption losses.

Expressions for f and χ have been established for spherical glass and quartz-type sand particles (see Appendix, Eq. A.6-A.9 respectively), via the heuristic fitting of data obtained by various authors normally within the ka range $10^{-1} – 10^{1}$. Attenuation data have typically been obtained from hydrophone measurements at fixed distances from the transmitting transducers, with the form function being calculated from backscatter measurements where the absolute measured pressure data are computed in equations comprising Bessel function terms [36]. Knowledge of the sediment specific f and χ are a prerequisite to facilitate suspended sediment concentration characterisation via single or dual-frequency inversion methods. Such algorithms enable solids concentration to be determined from acoustic backscatter measurements by inversion of the corresponding equation relating the two parameters (specifically Appendix Eq. A.1) [15, 25]. Importantly, there are currently limited data available in the literature for the determination of f and χ for many particles types other than glass beads and quartz-type sands (especially for particles with large density differences in the small ka range) although Moate and Thorne [37] have established values for a number of inorganic particles of mixed mineral composition.

The method outlined by Rice and co-workers [25] for determining ξ, considered a linearized rearrangement of the generally reported equation for root-mean-square voltage (see Appendix, Eq. A.1), in terms of the range-corrected echo amplitude (titled as the 'G-function') which is shown in Eq. 1. Here, k_t is the transducer constant, k_s is the sediment-specific scattering constant, V is the

measured voltage at a corresponding transducer range, r, and ψ is the near-field correction factor which accounts for the non-linearity of the acoustic wave within the transducer's near-field, and leads towards unity (1) in the far-field (which was assumed in the calculations herein). M is the solids concentration, while α_w and α_s quantify the attenuation due to water and sediment, respectively.

$$G = \ln(\psi r V) = \ln(k_s k_t) + \frac{1}{2} \ln M - 2r(\alpha_w + \alpha_s) \tag{1}$$

In the specific case of dispersion homogeneity with respect to particle size and concentration, taking the derivative with respect to r, then M, and utilising the definition of $\alpha_s = \xi^m M$ (see Appendix, Eq. A.3), an expression for ξ^m, the concentration independent attenuation coefficient, is obtained in homogenous dispersions, as given in Eq. 2 (where the superscript 'm' refers to it being a measured parameter).

$$\xi^m = -\frac{1}{2} \frac{d}{dM} \left[\frac{d}{dr} [\ln(\psi r V)] \right] = -\frac{1}{2} \frac{d^2 G}{dM dr} \tag{2}$$

Eq. 2 enables calculation of ξ^m directly from the gradient of dG/dr versus M. In this form, independent knowledge of the sediment is not a prerequisite, therefore ξ^m can be measured for any arbitrary system. Rearrangement of Eq. 1 and substitution of Eq. 2, also enables quantification of the sediment specific backscattering constant, k_s, for the same systems as shown in Eq. 3.

$$k_s = \frac{\psi r V}{k_t} M^{-\frac{1}{2}} e^{-2r(\alpha_w + \xi M)} \tag{3}$$

Eq. 1 is comparable to linearized expressions reported by other authors, such as Thorne and Buckingham [38], which provides a similar approach for calculating χ and f from the gradient and intercept of the linear curve of G versus r, respectively. However, the double differential arrangement (shown in Eq. 2) may lead to more robust estimations of the attenuation coefficient in concentrated engineering suspensions. In the case of Thorne and Buckingham [38], χ and f are quantified via echo profiles in dilute concentrations. In the present study, evaluation of the attenuation coefficient from a linear curve fit of dG/dr versus M [25], utilising measurements from a range of concentration profiles from dilute to concentrated, potentially reducing inaccuracies arising from data variability in complex sediments.

Additionally, estimations of the attenuation constant may be more accurate at higher particle concentrations, since attenuation begins to dominate over the scattering response of particles. It has been previously shown by Hunter and co-workers [28], that while acoustic backscatter strength versus particle concentration is only linear in dilute conditions, typically < 10 kgm^{-3} (depending on ka) signal attenuation remains linear into very concentrated conditions (> 50 kgm^{-3}), and thus measuring over this greater range enables enhanced accuracy of the attenuation coefficient. Since according to Eq. 2, dG/dr exhibits a linear relationship with respect to system attenuation, this suggests that similar concentration levels can be operated in the G-function method for accuracy. In fact, particle concentrations of up to 100 kgm^{-3} were used by Rice and co-workers [25] in a small-depth calibration chamber. The relationship is expected to retain linearity up to a certain concentration threshold, after which multiple scattering effects become significant. The threshold will lower with increasing frequency, due to heightened attenuation associated with a reduction in wavelength. Hay [39] observed this behaviour when comparing backscatter strength directly with concentration. Previously, the current authors have measured the ζ^m of highly attenuating barium sulphate particles, which were near-colloidal in size ($d_{50} = 7.8$ µm), in concentrations up to 64 kgm^{-3} within a 0.6 m depth vessel [26].

Rice and co-workers [25] also measured the combined backscattering-transducer constant K, defined in Eq. 4, where k_s is the particle scattering coefficient and k_t the transducer constant. Previous measurements were completed for glass beads and irregular plastic particles within a 41 – 691 µm size range [25, 32].

$$K = k_s k_t, \qquad\qquad\qquad\qquad\qquad\qquad (4)$$

Since k_t is an independent system constant that accounts for particular material electro-mechanical differences in specific transducer systems, it can be quantified by calibrating the transducer. Calibration can be achieved via measuring homogenous dispersions of scatterers, for which the backscattering and attenuating properties are well known (e.g. spherical glass particles) and rearranging the Eq. 5 for backscattered voltage response (see Appendix) solving for k_t, [40]. By combining calibration approaches, k_t can therefore be fully decoupled from Eq. 4, to enable independent quantification of k_s via Eq. 3. Once k_t is known for a particular transducer system, k_s can then be determined directly for any arbitrary dispersion (for experiments with the same transducers).

The methodology for determining ξ, k_s and k_t is outlined in the flowchart in Fig. 1, and exploits relatively few measurements of dispersions at different concentrations. Fig. 1 compares the measured process for obtaining these parameters (see Route 2), with the standard theoretical estimations for existing sediments (see Route 1). In Route 1, the attenuation coefficient and backscattering constant are calculated using values of f and χ derived from predetermined heuristic expressions given by Betteridge, Thorne and Cooke [40] for spherical glass particles (see Appendix, Eq. A.6-A.7), or Thorne and Meral [24] for sandy sediments (see Appendix, Eq. A.8-A.9). f and χ of a sediment are expressed with respect to ka. The superscript 'c' in Route 1 denotes parameters that have been calculated directly from these predetermined expressions. The superscript 'm' in Route 2 denotes parameters measured and determined via the G-function analysis. Firstly, ξ^m is measured directly (using Eq. 2). This parameter is combined with the calculated backscattering constant k_s^c and voltage data recorded in homogenous dispersions of known scatterers to determine the transducer constant k_t^m. Once k_t^m is determined from tests in large spherical glass dispersions of known properties, k_s^m can be determined by substituting the values of ξ^m and k_t^m into Eq. 3. This method measures the attenuation coefficient of the sediment directly, and does not require a predetermined expression for χ.

It is important to note that for calibration purposes, estimated attenuation coefficients are derived from expressions that only consider scattering losses. However, for systems within the Rayleigh regime, viscous losses may dominate, and overall measured values will be a summative of both types of loss ($\xi^m = \xi_s + \xi_{sv}$) where the subscript 's' relates to scattering and 'sv' to viscous losses respectively. Theoretical models for ξ_{sv} have been developed by Urick [41], as summarised by Guerrero et al. [12], and are shown in Eqs. 5 – 8. Here, ξ^c_{sv}, is the calculated viscous attenuation loss for a monosized spheres of radius a, v is the kinematic viscosity of the fluid (given as for water at 15 degrees centigrade, 1.1×10^{-6} m^{2}s^{-1} [12]), σ is the particle to fluid density ratio, and again k is the wavenumber, while ρ_s is the density of the particle phase (kgm^{-3}) and F is the frequency of the transmitted pulse (Hz) T', γ, and s are intermediate variables in the calculations. These expressions allow estimation of the viscous attenuation, to compare to overall measured values.

$$\gamma = \sqrt{\frac{\pi \cdot F}{\upsilon}} \tag{5}$$

$$s = \frac{9}{4 \cdot \gamma \cdot a}\left(1 + \frac{1}{\lambda \cdot a}\right) \tag{6}$$

$$T' = 0.5 + \frac{9}{2 \cdot \gamma \cdot a} \tag{7}$$

$$\xi_{sv}^{c} = \frac{k}{2\rho_{s}}(\sigma-1)^{2}\left(\frac{s}{s+(\sigma+T')^{2}}\right) \tag{8}$$

3 Materials and methods

3.1 Materials

Calibrations were conducted via two sizes of glass beads; Honite 16 and Honite 22 (Guyson International Ltd, UK). Acoustic constants were determined for glass beads and a range of additional sediments: barium sulphate or barytes (RBH Ltd, UK), titanium dioxide or titania (Degussa, Germany), poly-methyl methacrylate (pMMA) latex particles and methyl methacrylate (MMA) emulsions. The MMA emulsions and latex particles were manufactured in-house via a crossflow membrane emulsification (XME) technology and subsequent suspension polymerization, as outlined in a previous publication [42]. Initially, 2 L of MMA emulsion at 30 wt.% were produced. Subsequently, 1 L of emulsion was diluted with 1 L of sodium dodecyl sulfate (SDS)-laced water, and polymerized to generate 2 L of pMMA suspension at 15 wt.%. This dispersion was diluted to obtain measurements at a range of concentrations.

3.2 Particle characterization methods

The size distributions of each particle type were obtained from a minimum of three sample runs each in the Malvern Mastersizer 2000 laser diffractometer (Malvern Instruments, UK). Particle images were obtained via the LEO/Zeiss 1530 FEGSEM (LEO Elektronike GmbH, Germany) or the Carl Zeiss EVO MA15 (Carl Zeiss Ltd, UK) scanning electron microscopes. The densities of Honite 16, Honite 22, barytes and titania were measured via a Accu-Pyc 1330 helium pycnometer (Micrometrics Instrument Corporation, USA), from a minimum of three powdered samples each.

3.3 Acoustic calibration methodology

The principles of calibration are similar to those reported by Thorne and Hanes [15] and Betteridge, Thorne and Cooke [40], albeit with some differences with respect to concentration, particle size and pulse emission rate. Firstly, the calibration procedure was streamlined by measuring intermediate concentrations in the range of $0.5 - 10$ kgm^{-3}, with the aim of reducing data variability due to random fluctuations that are inherently more likely with dilute dispersions as fewer scatterers are present [43]. As such, small particle radii (< 40 µm) whose attenuation coefficients fall within the attenuation curve minima between strong viscous and scattering attenuation behaviour [13] were able to be measured with a relatively high degree of stability (signal strength variation $< 3 - 5\%$ typical). Pulse emission rates were also increased from typical low rates around 4 Hz [15, 40] to 32 Hz. This intensification reduced the required capture times to ~10 minutes, whilst still enabling sufficient time for stray reflection dissipation between each pulse.

A Perspex column with dimensions 0.3 m diameter x 0.8 m height, and 4 x 0.02 m thick baffles of full tank height, was employed in all experiments (as shown in Fig. 2). The waterline was set at 0.6 m and an impeller, mixing at a rate of 1600 rpm, was positioned off-centre, 0.1 m above the base. In this set-up, depth-wise concentration homogeneity was tested and established (see for example from previous literature, profiles of dense barytes particles in suspension, where sample standard deviations were in the range $\pm 0.005 - 0.127$ wt.% [26]). Additional homogeneity checks were performed via sampling and the calculation of wet-dry ratios at each concentration for all particle types. A smaller Perspex column with dimensions 0.11 m diameter x 0.33 m height was utilised for measuring latex suspensions and emulsions, as smaller particle volumes ($1 - 2$ L) were available for measurement. The corresponding dispersions were mixed via a magnetic stirrer operating with waterlines at either 0.15 or 0.25 m. Due to the relatively low density of the latex particles, homogenisation with a high shear overhead stirrer was not required in this case.

An AQUAscat 1000 (Aquatec Group Ltd, UK) acoustic backscattering system (ABS) was used in all experiments, with 3 transducer set combinations: Set 1: 1, 2, and 4 MHz; Set 2: 1, 2, 4 and 5 MHz; Set 3: 1 and 2 MHz.. The travel time between the instrument emitting a pulse and receiving the corresponding echo is of the order of 0.8 x 10^{-3} s at a 32 Hz pulse repetition frequency. Depth measurements were segregated into 2.5 mm bins, which corresponds with the resolution limit of

the instrument. An average backscatter voltage versus depth profile was recorded by the ABS per second, derived from the 32 individual measurements taken per second. The backscatter voltage data are recorded in root-mean-square format. The tank was initially degassed and each dispersion was mixed for ten minutes after sediment addition and prior to ABS measurements. Measurements were taken with each transducer set, with three measurements implemented per transducer for a duration of ten minutes each. For data analysis, the average of 3 x 10 minute profiles was taken per transducer, to reduce influences of noise inherent within a dynamic suspension system.

4   Results and discussion

4.1   Particle characterization

The cumulative size distributions of each of the particle systems investigated are presented in Fig. 3. The Honite glass beads, which are the largest in size, have narrow size distributions, making them ideal as calibration species. The coefficient of variation (CV, being the ratio of the standard deviation to the mean, quoted in this paper as a fraction) for both glass systems was ~0.2, highlighting their relative monodispersity. The pMMA latex beads and the MMA droplets, which are close to colloidal in size, had slightly broader distributions, with CV = 0.7. The size range of barytes is larger than the pMMA (although still largely below 10 µm) and were notably more polydisperse than the latex particles, having a CV = 1.5. The titania had the highest level of polydispersity (CV = 5), and in fact, it is known they are highly aggregated structures in suspension, comprising a fraction of colloidal particles, intermediately sized aggregates and a fraction of larger clusters [27]. In addition to the high polydispersity, such structuring may suggest potential complexities in their acoustical scattering behaviour, due to the influence of the primary particles on the overall scattering of the aggregate [44-46]. SEM images of the particles provided in Fig. 4 confirm the size characteristics observed in Fig. 3, and additionally highlight the shape features of each powder. While the Honite glasses (a) to (b) and the latex (e) are spherical, the barytes (c) is irregularly shaped, whereas the titania particles (d) are spheroidal aggregated clusters (consistent with their polydisperse size, as discussed).

Shape, size and material density, are all important features acoustically because they govern the type of scattering and attenuation mechanisms observed upon insonification. These characteristics are collated in Table 1, from the largest to smallest median diameter (d_{50}). The size range of the

particles, which are insonified with frequencies within the megahertz range, enable acoustic investigation within the Rayleigh regime, where ka < 1. In fact, due to the colloidal size of the MMA and pMMA beads, it is possible to investigate the region of ka < 10^{-1}, for which the data in the literature are very limited. In Table 1, the particle types are ordered according to the dominant attenuating mechanism. Scattering attenuation is the primary mechanism in the case of larger Honite particles. For the small and dense particles (barytes and titania) viscous losses are assumed to dominate due to the inertia of the particle, as there is a sizeable density contrast between the particle and fluid. However, where the density contrast between a small particle and fluid is low, and there are differences in the thermal properties of the two phases, as in the case of MMA and pMMA, there is heat flow across the fluid-particle interface, resulting in thermoacoustic losses [33]. These mechanisms strongly influence the intensity and attenuation of the backscattered pulse. Hence, they have direct implications on application capability of the ABS with respect to the types of suspensions that are measurable, and the possible penetration depths [47].

4.2 Comparison of backscatter and attenuation responses of various particle dispersions

The backscatter intensity profiles of pMMA dispersions at 1.0, 3.7 and 7.3 vol%, are presented in Fig. 5(a-b) for 1 and 2 MHz respectively, in terms of (I) decibel intensity, and (II) the linearized G-function, with respect to transducer range r. Initially, the backscatter intensity fluctuates in a series of peaks and troughs due to natural perturbations in the phase of the received waves in the transducer's near-field range, until the transducer focal point (denoted by the vertical dotted lines in Fig. 5). The intensity subsequently decreases monotonically with distance, consistent with attenuation-dominated systems [26-29], followed by an intense peak marking the column base at the furthermost measured transducer range.

Comparing the backscatter response between the 1 and 2 MHz frequencies in Fig 5 (I) indicates some similarities and differences to previous measurements on inorganic mineral systems comprising small particle sizes. [26, 27]. Attenuation increases from 1 to 2 MHz as would be expected [28], due to its natural enhancement with decreasing wavelength. However, the relative difference in attenuation magnitude is not as significant as would be expected for the doubling in signal frequency [48]. In this case, the densities of the organic dispersions are low and are

12

comparable to that of the dispersing fluid, water. Hence, signal losses may be primarily a result of thermoacoustic attenuation, rather than viscous or scattering attenuation which are the dominant mechanisms for the inorganic particles investigated. Specifically, the thickness of the thermal layer generated around a particle upon insonification is proportional to the reciprocal square-root of the frequency [9, 33]. Therefore, a low frequency gives rise to a longer thermoacoustic wave, in which case there is potential for the overlapping of thermal layers between neighbouring particles, that may reduce the temperature gradient at any given particle interface and overall energy loss. Indeed, the significant intensity reduction between the 1 and 2 MHz data in Fig. 5, suggests that higher frequencies would not be suitable for application in organic dispersions, where an appreciable penetration depth of tens of centimetres is required for measurement, thus constraining the range of usable frequencies.

The G-function response versus distance in Fig. 5(II) is qualitatively similar to the decibel backscatter profiles, due to the dispersions being attenuation-dominated giving a linear trend outside of the near-field region as expected [25]. However, it is noted that the gradient of the profiles for both frequencies are low in magnitude at all but the highest concentration (where an increase in gradient is indicative of higher attenuation). This trend highlights that the G-function has reduced sensitivity for correlating the attenuation of the particles at lower concentrations. Specifically, dG/dr has a gradient of lower magnitude than the directly interpolated attenuation (dB/m) taken from the measured backscatter intensity versus distance, for the same concentration.

The general backscatter intensity results of these colloidal organic particles are weak compared to those exhibited by near colloidal inorganic barytes [26] and titania suspension [27] systems. This behaviour is partly a function of particle size, where the pMMA particles are the smallest of the particle systems tested here, whereas the minerals are intermediate and the glass beads are the largest (refer to Table 1). Thus, the scattering cross-sections of the colloidal organics are relatively very small. Nonetheless, the organic dispersions are indeed measurable at 15-20 cm depths, which in itself is a significant result for ABS application, demonstrating its capability in very weakly-scattering dispersions.

13

The general G-function profiles of pMMA at 1 vol% are also compared with the MMA emulsions and the other mineral particle systems studied; titania, barytes and Honite 22, in Fig. 6. It is noted that the raw backscatter data for the Honite 22 is given within the Supplementary Materials (Fig. S1 (b)), while raw backscatter data for the titania are taken from [27]. The actual values of G are representative of the amount of acoustic backscatter, with the Honite-22 exhibiting higher values due to its larger size and thus scattering cross-section [38]. The slope of the decay of G with distance is representative of the amount of signal attenuation (as discussed), where it is clear that the pMMA and MMA have lower total attenuation in comparison to the similarly-sized barytes and titania particles, at the same concentration. The attenuating behaviour of each particle system is compared in Fig. 7, where the gradients, dG/dr, of the 2 MHz G-function (shown at one concentration in Fig. 6) are plotted with respect to concentration M. Linear regression lines are presented alongside data points. Again, the raw Honite 22 backscatter intensity profiles and the corresponding G-function profiles from which the dG/dr profiles were derived are provided in the Supplementary Materials (Figs. S1 and S2, respectively). Honite 16 data are also provided in the Supplementary Materials, however they were omitted from the plot in Fig. 7 for brevity. The dG/dr profiles for titania and barytes were derived from previously data published by the current authors [26, 27]. For MMA and pMMA analysis, the data in Fig. S3 and Fig. 5 are respectively utilised.

The inorganic particle data in Fig. 7 display highly linear trends in the G-function gradient with respect to concentration. Honite 22, the larger of the plotted scatterers, attenuates the acoustic pulse minimally with respect to the inorganic minerals and the organic latex. Its size makes it well suited to generate intense acoustic backscattered signals, yet it is not so large that scattering attenuation becomes significant [13]. This observation is further validated upon comparison of the associated sediment attenuation coefficients listed in Table 2. ξ^m of each particle system was determined via the substitution of the gradient of dG/dr versus M in Fig. 7, into Eq. 2. The resulting frequency-specific attenuation coefficients of Honite 16 are greater than those of Honite 22, as Honite 16 is within the size range at which scattering attenuation effects are enhanced [13].

The sediment attenuation coefficients of titania and barytes are approximately an order of magnitude greater than those of the Honite beads (see Table 2). The enhanced attenuation is primarily due to the small scattering diameters and high density contrast generating significant

viscous drag between the mineral and water phases [26, 27]. While the MMA and pMMA particles are colloidal and thus smallest in size, they are less attenuating than the similarly sized inorganic minerals. This reduction is likely a result of their relatively low density, which reduces viscous absorption, although further data points are required in Fig. 7 from a wider concentration range to fully validate the attenuation coefficients of MMA and pMMA. The relatively low volume of the emulsion and particles produced from crossflow membrane emulsification and suspension polymerization limited further experiments, but is an area of ongoing work.

4.3 Transducer constants and dimensionless scattering relationships for glass dispersions

The probe-specific transducer constants, k_t^m, were determined by substituting V_{RMS} data recorded at dilute to intermediate dispersion concentrations into the V_{RMS} equation (see Appendix, Eq. A.1) with respect to transducer range r. Additional parameters substituted into the equation include α from the measured ξ^m (see previous discussion) and k_s^c, predicted from the Betteridge, Thorne and Cooke [40] heuristic expressions (see Appendix, Eqs. A.5 and A.6). This alternative analysis process corresponds with Route 2 in the flowchart in Fig. 1.

As an example, Fig. 8 presents k_t^m with respect to r, determined at one dilute and one intermediate dispersion concentration of Honite 16 and Honite 22, for a 2 MHz probe. As k_t is a system parameter which relates to the transducer and cable properties, it should therefore be independent of any dispersion related factors such as particle size, concentration or distance from transducer. In all cases, the data in Fig. 8 show that k_t^m here is independent of r, which would be expected for well mixed homogeneous dispersions. Also, there are only minor variations in the data between each concentration and size investigated in the dynamically mixing dispersions. For example, the average value of k_t^m from the data in Fig. 8 for the Set 2, 2 MHz probe is 0.0077 ± 0.0010.

Average k_t^m values were determined for all probe sets and all frequencies and are presented in Table 3. For comparison, the values of k_t^c, which were calculated from V_{RMS} data are provided, alongside parameters ξ^c and k_s^c obtained directly from the Betteridge, Thorne and Cooke [40] heuristic expressions for χ and f (see Appendix, Eqs. A.6-A.7). This standard analysis corresponds with Route 1 in Fig.1. The values of k_t^m and k_t^c compare well, with differences of the order of 10%.

Importantly, the consistency in these results indicate that streamlining the calibration process by utilizing high pulse-emission rates (~32 Hz) and intermediate concentrations (up to ~10 kgm^{-3}) is a valid option for determining k_t. Confidence is also provided in the G-function approach for determining attenuation constants of particles from direct measurement.

For completeness, the backscattering constant, k_s^m, was determined by substituting measured values of ζ^m and k_t^m into the V_{RMS} equation defined in the Appendix (Eq. A.1, and the final step in Route 2 in the flowchart in Fig. 1). k_s^m is given in Fig. 9 for Honite 16 and Honite 22 at one dilute and one intermediate concentration for the Set 2, 2 MHz probe as an example. The values for Honite 16 and Honite 22 vary, where the larger Honite 16 particles exhibit the largest k_s^m, as expected. In both cases, k_s^m is invariant with distance and the data at dilute and intermediate concentrations align well, highlighting that both systems are at concentrations low enough that significant interparticle scattering does not occur (which would interfere with calculated values at higher concentrations and or depths). Measured values of k_s^m are compared with predicted values of k_s^c in Table 2. The average measured and predicted backscattering constants of Honite 16 and Honite 22 align well. The data presented for each particle type in Table 2 also demonstrate the expected increase in the magnitude of the backscattering constant with increasing particle size and frequency [13].

The measured backscattering constants k_s^m given in Table 2 were substituted into the equation relating k_s with the dimensionless form function f (see Appendix, Eq. A.5). Typically, f is calculated from heuristic expressions for glass spheres [40] or sandy sediments [24]. The values of f derived from k_s^m here are compared with those calculated directly from the heuristic expressions in Fig. 10(a) in the low-ka (Rayleigh scattering) regime. The measured data align well with the heuristically calculated model for glass spheres [40], however the data are offset with respect to the model for roughened sandy particles [24]. Since the Honite particles are largely spherical, this result perhaps is not surprising. It is noted also that the closeness of fit between the data and the spherical model highlights that there are no measureable effects from polydispersity in the glass systems, which was expected given the low CV value (~0.2) discussed.

The measured sediment attenuation coefficients given in Table 2 (discussed in Section 4.2) were then substituted into the equation relating ξ with the total normalised scattering cross-section χ (see Appendix, Eq. A.4), which quantifies the attenuation behaviour in dimensionless form. Similarly, the form function χ is calculated from heuristic expressions for glass spheres [40] or sandy sediments [24]. However, direct measurement of ξ enabled measured calculation of χ here. Fig. 10(b) compares these values in the low-ka range.

The measured scattering cross-sections align well with predicted values at ka > 0.5, as do the values of ξ^m with ξ^c predicted via the Betteridge, Thorne and Cooke [40] heuristic expressions in Table 2. However, data deviate from prediction in the region ka < 0.5, which corresponds with the insonification of smaller particles (Fig. 10b). Here, the heuristic expressions under-predict ξ and thus χ, by up to an order of magnitude. Given that the close correlations of k_s (Fig. 10 (a)) indicated no substantial effects from polydispersity, the inconsistency between the data and predicted relationship is most likely due to viscous absorption effects becoming significant for the Honite 22 particles, as these are known to dominate within the low-ka region [12, 49], and are not directly accounted for in the scattering models of attenuation [24, 40].

Previous work by Thorne, MacDonald and Vincent [44] has looked to adapt the Betteridge, Thorne and Cooke [40] model to account for viscous effects which dominate at small grain sizes. The resulting hybrid model does not predict a monotonic dependence of χ with respect to ka in the Rayleigh regime, but a rather more complex relationship which initially decreases in the region $10^{-1} <$ ka $< 10^0$, gradually increases ($10^{-2} <$ ka $< 10^{-1}$) and finally decreases ($10^{-2} <$ ka $< 10^{-4}$). The hybrid model for determining f and χ has been utilised with success in field studies by Sahin, Verney, Sheremet and Voulgaris [50] to estimate suspended sediment concentration of flocculated dispersions which comprise small particles. It is also possible to directly estimate the viscous attenuation for spherical particles using the model of Urick [41] (as summarized by Guerrero et al. [12] and described in Section 2). Indeed, viscous attenuation calculations using the Urick model were attempted for various particle systems in the Rayleigh regime, and are discussed in Section 4.4.

4.4 Density-normalised form function and total normalised scattering cross-section

As discussed within Section 4.2, the attenuation constants for a range of sediment types were determined via the G-function analysis [25] for colloidal, organic and aggregated particulates. By using the methodology outlined in Fig. 1 flowchart Route 2 (and described in relation to Honite glass particles in Section 4.3) the scattering constants were similarly determined for all particle types. This information is given in Table 2. It is noted that the scattering constants could not be determined for the MMA emulsion droplets due to data fitting variability (inherent in low-intensity backscatter measurements) and these were ignored hereafter.

With both scattering and attenuation constants, the dimensionless form function f and total scattering cross-section χ could be constructed for all particle systems and frequencies, the key goal being to normalise the various data sets. The scattering behaviour of each particle type is expected to be highly dependent on the density, because χ is proportional to the density and f varies as the square-root of density (refer to Appendix Eqs. A.4-A.5). Since a large range of particulate densities were investigated, it was therefore used as the dependent variable. Accordingly, f and χ for each sediment was compared according to their specific gravity ϱ to retain non-dimensionality, and is shown in Fig. 11(a-b) versus ka respectively (with $f/\sqrt{\varrho}$ and χ/ϱ).

The dashed lines depicting predicted data in Fig. 11 correspond with modified f and χ expressions, as calculated from the Betteridge, Thorne and Cooke [40] model that have also been corrected for density in the given relationships ($f/\sqrt{\varrho}$ and χ/ϱ). These are similar to functions reported by Moate and Thorne [37], as used by Wilson and Hay [51], who also investigated particle types with a range of densities, although there are some key differences. Moate and Thorne [37] normalised f and χ by the grain density and not the density ratio (as has been done here) and therefore did not strictly retain non-dimensionality. Additionally, those authors generally investigated larger particle sizes, reporting χ for ka > 1 and f for ka > 10^{-1}.

For most systems, the data given in Fig. 11 are relatively consistent, enabling direct comparison of particles with a range of properties, and it is important to consider the effect of density normalisation. The augmented form function, $f/\sqrt{\varrho}$, appears to collapse almost all particle

dispersions approximately onto a single relationship versus ka (Fig. 11a). The one particle type that clearly does not fit the trend is titania. One significant reason for this result may be the agglomerated nature of the particles, which will lead to a complex acoustic scattering response that cannot be accounted for from density differences alone [45, 46]. It is also evident from the form function that measured data considerably over-predict the estimated scattering relationship at very low ka. It is believed that the most likely explanation for the deviation is suspension polydispersity effects. While such effects were not evident in the relatively monodisperse glass suspensions, the increasing particle spread of the barytes and latex particles for example (relative CV ratios of 0.7 and 1.5 respectively) would imply greater influence in these systems.

Thorne and Meral [24] considered acoustic backscatter data at different set CV levels, and highlighted the influence of polydispersity on increasing measured form factor values. They formed an empirical correlation to take account of these effects for both the form function and scattering cross-section, which is described in the Appendix, Eqs. A.10 and A.11 respectively. By utilising Eq. A.10, the calculated normalised form factor values were re-estimated, for particles of the same size and CV ratios as the latex and barytes. These values are compared to the direct measurements at multiple frequencies in Table 4. Importantly, the corrected estimated factors for barytes are now very similar to the measured values. The estimations of latex are now also more closely correlated with those measured (to within an order of magnitude) however there are still discrepancies; although, it is emphasised that that the relationship was based on data at fixed and relatively low total CV levels, and ka between 10^{-1}-10^{0} [24]. It may be that the influence of polydispersity increasingly dominates the scattering response as ka is reduced.

Another consideration is the level of accuracy for measurements in the very low-ka range. As previously discussed in relation to the pMMA particles (Fig. 5), due to their small size, measured backscatter strengths and dG/dr values were relatively low, and because of the lower scattering intensity, instrument sensitivity in this region may also be reduced. Indeed, it has been noted in previous studies of suspension attenuation in the low-ka range that measurements are also complicated by the increasing relative influence of the solvent attenuation [43] which may provide a further complication for characterising similar colloidal systems.

The data for the cross-section χ (Fig. 11b) suggests a weaker density-normalised correlation, with noticeably more scatter in the data at the low-ka region, which may have a number of causes. The roles of particle properties such as shape, orientation, aggregation state, surface roughness and cavities, for example, can cause deviation in the attenuation behaviour of non-spherical particles relative to that estimated using expressions for spherical particles with the same equivalent diameter [13, 52, 53]. These are further complexities that this density normalisation is unable to fully capture, especially in the case of titania and barytes. Effects of polydispersity on the scattering cross-section may also be evident in measured values [12]; however, it is thought that the most significant contribution to variations at low ka will be due to the complex modes of attenuation in this region, where viscous and even thermal losses may dominate (as discussed in relation to the glass only data in Fig. 10b). To better illustrate these effects, the measured attenuation constants (ζ^m) reported in Table 3, were compared to values estimated from viscous attenuation alone (ζ^c_{sv}) using Eqs. 5-8 [12, 41], for the pMMA, barytes, Honite 22 and Honite 16 suspensions, as presented in Fig. 12.

The attenuation constant comparisons in Fig. 12 highlight a number of important features. It is evident that the measured values from Honite 16 are an order of magnitude larger than those estimated from viscous absorption, which would be expected, given that attenuation for particles of this size is mainly through scattering, and confirms that these are a good choice for calibration. For the Honite 22, data from the 1 and 2 MHz probes (smallest values) are only just above those estimated from viscous absorption, indicating that viscous absorption does indeed dominate for particles of this size (~40 µm) and below, apart from at the highest frequencies (4 MHz, highest value shown) where scattering attenuation is heightened.

For the dense, fine barytes, measured attenuation constants also correlate very closely with those predicted from viscous attenuation, and values generally are large due to their density. It is noted that the close correlation also suggests a relatively weak effect of greater particle size distribution in relation to the form function values (as discussed earlier and shown in Fig. 11a). The equation given in the appendix to account for particle size distribution on attenuation coefficients (Eq. A.11) is for scattering attenuation only, and is therefore not applicable in this case. The influence of particle size distribution on viscous attenuation from the literature is less clear; however, in

measurements on fine silt particles, work from Guerrero et al. [12] would predict a reduction in the magnitude of measured values, although significantly only for very fine particles < 5 μm. Lastly, it is clear that measured attenuation constant values for the pMMA particles are also significantly above those estimated from viscous attenuation (given their low relative density), despite their small size. This difference would further suggest that these particles undergo enhanced thermoacoustic attenuation [9, 33].

5   Conclusion

A rapid, phenomenological analysis methodology utilising in situ acoustic backscatter measurements to determine the acoustic backscattering (k_s) and attenuation constants (ξ) for arbitrary particle types is reported. The approach considered the double differential of a linearised expression for the backscatter voltage known as the G-function, as outlined by Rice and co-workers [25], to quantify ξ directly for any particle type. Subsequently, a streamlined approach for transducer calibration was presented and validated with glass dispersions, which utilised known expressions for spherical particles, to measure the transducer constants (k_t) for each probe and corresponding frequency, enabling extraction of k_s values for all particle types. Subsequently, f and χ were calculated via substitution of measured values of k_s and ξ into the corresponding equations.

A number of particle types were investigated, including organic latex particles and dense fine minerals (titania and barytes) in comparison to spherical glass. A particular focus was given to the measurement of MMA emulsions and pMMA dispersions, owing to their widespread use in the personal care and chemical industries. While their relatively low density and close-to-colloidal size (1 – 10 μm) produced acoustic signals close to the lower instrumental limit, these dispersions were characterised successfully and their acoustic properties measured. These measurements highlight the technique's ability to obtain data in the low-ka region of the Rayleigh scattering regime, to facilitate characterisation of industrially relevant particles.

The dimensionless scattering and attenuation properties of this diverse range of particles were compared directly via density ratio normalisation. The form function of all particle types were found to align at low ka, with the exception of titania because of scattering complexities associated

21

with agglomerated particles. Deviations from expected scattering trends were also considered to be due to the influence of polydispersity. There was lower consistency in the measured cross-section data from density-normalised predictions at low ka, most likely due to the increasing influence of viscous attenuation. Comparison between measured values and estimates of viscous attenuation highlighted this trend, and further suggested the latex particles are dominated by thermoacoustic attenuation, which is not evident in the mineral particles. Generally, the normalised scattering relationships provide a clear indication that particles close to the colloidal regime can be measured successfully with acoustic backscatter systems, and highlight the great potential of this technique to be applied for in situ or online monitoring purposes in such systems.

Acknowledgements

APPENDIX

The acoustic backscattering model described by Thorne and Hanes [15], is summarised here. The root-mean-square of excitation voltage, V_{RMS}, from the received backscattered pressure wave, varies with transducer range, r, and concentration of suspended sediment, M, as described in Eq. A.1. Here, k_t is the independent transducer constant, the backscattering constant k_s, denotes the backscattering properties of the sediment, while the attenuation coefficient $\alpha = \alpha_w + \alpha_s$, quantifies the sound attenuation due to absorption and scattering losses imparted by the fluid α_w and sediment α_s.

$$V_{RMS} = \frac{k_s k_t}{\psi r} M^{\frac{1}{2}} e^{2r\alpha} \tag{A.1}$$

The attenuation contribution of water at zero salinity is taken from [25], at a temperature T in °C for a given ultrasonic frequency F, as shown by Eq. A.2.

$$\alpha_w = 0.05641 F^2 e^{-\left(\frac{T}{27}\right)}. \tag{A.2}$$

The near-field correction factor, ψ, accounts for the non-linearity of the acoustic wave within the transducer's near-field range, and tends to unity (1) in the far-field (as approximated for this study). The sediment attenuation, α_s, is given in Eq. A.3, as an integral over the insonified distance, r, where ξ is the concentration-independent sediment attenuation coefficient. If particle size and concentration are invariant throughout the measured depth, r (assuming well mixed conditions) then $\alpha_s = \xi M$.

$$\alpha_s = \frac{1}{r} \int_0^r \xi M dr \tag{A.3}$$

ξ is related from the total normalised scattering cross-section χ, sediment radius, a, and sediment density, ρ, as given in Eq. A.4 (true for systems that are scattering dominant). It is noted that the scattering cross-section χ, is dimensionless, and is often compared against ka (where k is the wavenumber, and a is the particle radius).

$$\xi = \frac{3\chi}{4\rho a} \tag{A.4}$$

The particle scattering coefficient, k_s, can similarly be related to the dimensionless scattering form function, f, as well as the sediment density and particle size, as given in Eq. A.5.

$$k_s = \frac{f}{\sqrt{a\rho}} \tag{A.5}$$

Empirical expressions for f and χ are given by Betteridge et al. [40] for spherical glass particles, as given in Eq. A.6 and A.7.

$$f = \frac{\left(1-0.5e^{-((ka-1.5)/0.5)^2}\right)\left(1+0.4e^{-((ka-1.5)/3.0)^2}\right)\left(1-0.5e^{-((ka-5.9)/0.7)^2}\right)(ka)^2}{1.7+0.95(ka)^2} \tag{A.6}$$

$$\chi = \frac{0.24\left(1-0.4e^{-((ka-5.5)/2.5)^2}\right)(ka)^4}{0.7+0.3(ka)+2.1(ka)^2-0.7(ka)^3+0.3(ka)^4} \tag{A.7}$$

Thorne and Meral [24] derived alternative expressions for quartz-type sand particles, as given in Eq. A.8 and A.9.

$$f = \frac{ka\left(1-0.35e^{-((ka-1.5)/0.7)^2}\right)\left(1+0.5e^{-((ka-1.8)/2.2)^2}\right)}{1+0.9(ka)^2} \tag{A.8}$$

$$\chi = \frac{0.29(ka)^4}{0.95+1.28(ka)^2+0.25(ka)^4} \tag{A.9}$$

These expressions for the scattering and attenuation properties of suspensions are strictly only true for monodisperse systems, but are normally correlated experimentally to dispersions within a single sieve fraction (a $^{+}$/- 0.09a) [24]. Thorne and Meral [24] also investigated the influence of particle size distribution, by measuring the enhancement of f and χ for systems with known coefficients of variation. Resulting fitted expressions, giving the ratio of average measured values in relation to those estimated from monodisperse systems of moderate variation in the Rayleigh regime, are shown in Eq. A.10 and A.11. Here, $<f>$ and $<\chi>$ are the averaged values for systems with a given distribution in relation to their respective monodisperse values, and CV is the coefficient of variation, quoted as a fraction (tested for systems where $CV = 0.4$ [24]).

$$\frac{\langle f \rangle}{f} = \sqrt{\frac{1 + 15CV^2 + 45CV^4 + 15CV^6}{1 + 3CV^2}}$$ (A.10)

$$\frac{\langle \chi \rangle}{\chi} = \frac{1 + 15CV^2 + 45CV^4 + 15CV^6}{1 + 3CV^2}$$ (A.11)

References

[1] R. Meral, Laboratory Evaluation of Acoustic Backscatter and LISST Methods for Measurement of Suspended Sediments, Sensors, 8 (2008) 979-993.

[2] L. Hernando, A. Omari, D. Reungoat, Experimental investigation of batch sedimentation of concentrated bidisperse suspensions, Powder Technol., 275 (2015) 273-279.

[3] D.C. Fugate, C.T. Friedrichs, Determining concentration and fall velocity of estuarine particle populations using ADV, OBS and LISST, Cont. Shelf Res., 22 (2002) 1867-1886.

[4] G.T. Bolton, M. Bennett, M. Wang, C. Qiu, M. Wright, K.M. Primrose, S.J. Stanley, D. Rhodes, Development of an electrical tomographic system for operation in a remote, acidic and radioactive environment, Chem. Eng. J., 130 (2007) 165-169.

[5] L. Liu, R. Li, S. Collins, X. Wang, R. Tweedie, K. Primrose, Ultrasound spectroscopy and electrical resistance tomography for online characterisation of concentrated emulsions in crossflow membrane emulsifications, Powder Technol., 213 (2011) 123-131.

[6] D.R. Kaushal, Y. Tomita, Experimental investigation for near-wall lift of coarser particles in slurry pipeline using γ-ray densitometer, Powder Technol., 172 (2007) 177-187.

[7] C.P. Chu, S.P. Ju, D.J. Lee, F.M. Tiller, K.K. Mohanty, Y.C. Chang, Batch settling of flocculated clay slurry, Ind. Eng. Chem. Res., 41 (2002) 1227-1233.

[8] A.S. Dukhin, P.J. Goetz, Acoustic and electroacoustic spectroscopy for characterizing concentrated dispersions and emulsions, Adv. Colloid Interfac. Sci., 92 (2001) 73-132.

[9] T. Hazlehurst, O. Harlen, M. Holmes, M. Povey, Multiple scattering in dispersions, for long wavelength thermoacoustic solutions, J. Phys. Conf. Ser., 498 (2014) 012005.

[10] M.J.W. Povey, Acoustic methods for particle characterisation, KONA, 24 (2006) 126-133.

[11] A. Rodriguez-Molares, C. Howard, A. Zander, Determination of biomass concentration by measurement of ultrasonic attenuation, Applied Acoustics, 81 (2014) 26-30.

[12] M. Guerrero, N. Rüther, R. Szupiany, S. Haun, S. Baranya, F. Latosinski, The acoustic properties of suspended sediment in large rivers: consequences on ADCP methods applicability, Water, 8 (2016) 13.

[13] S.A. Moore, J. Le Coz, D. Hurther, A. Paquier, Using multi-frequency acoustic attenuation to monitor grain size and concentration of suspended sediment in rivers, J. Acoust. Soc. Am., 133 (2013) 1959-1970.

[14] S.M. Simmons, D.R. Parsons, J.L. Best, K.A. Oberg, J.A. Czuba, G.M. Keevil, An evaluation of the use of a multibeam echo-sounder for observations of suspended sediment, Applied Acoustics, 126 (2017) 81-90.

[15] P.D. Thorne, D.M. Hanes, A review of acoustic measurement of small-scale sediment processes, Cont. Shelf Res., 22 (2002) 603-632.

[16] W.O. Carpenter, B.T. Goodwiller, J.P. Chambers, D.G. Wren, R.A. Kuhnle, Acoustic measurement of suspensions of clay and silt particles using single frequency attenuation and backscatter, Applied Acoustics, 85 (2014) 123-129.

[17] D. Kosior, E. Ngo, T. Dabros, Determination of settling rate of aggregates using ultrasound method during paraffinic froth treatment, Energ. Fuel, 30 (2016) 8192-8199.

[18] T. Norisuye, Structures and dynamics of microparticles in suspension studied using ultrasound scattering techniques, Polym. Int., 66 (2017) 175-186.

[19] J.F. Stener, J.E. Carlson, A. Sand, B.I. Pålsson, Monitoring mineral slurry flow using pulse-echo ultrasound, Flow Meas. Instrum., 50 (2016) 135-146.

[20] R. Weser, S. Wöckel, B. Wessely, U. Hempel, Particle characterisation in highly concentrated dispersions using ultrasonic backscattering method, Ultrasonics, 53 (2013) 706-716.

[21] R. Weser, S. Woeckel, B. Wessely, U. Steinmann, F. Babick, M. Stintz, Ultrasonic backscattering method for in-situ characterisation of concentrated dispersions, Powder Technol., 268 (2014) 177-190.

[22] X.-j. Zou, Z.-m. Ma, X.-h. Zhao, X.-y. Hu, W.-l. Tao, B-scan ultrasound imaging measurement of suspended sediment concentration and its vertical distribution, Meas. Sci. Technol., 25 (2014) 115303.

[23] P.D. Thorne, D. Hurther, B.D. Moate, Acoustic inversions for measuring boundary layer suspended sediment processes, J. Acoust. Soc. Am., 130 (2011) 1188-1200.

[24] P.D. Thorne, R. Meral, Formulations for the scattering properties of suspended sandy sediments for use in the application of acoustics to sediment transport processes, Cont. Shelf Res., 28 (2008) 309-317.

[25] H.P. Rice, M. Fairweather, T.N. Hunter, B. Mahmoud, S. Biggs, J. Peakall, Measuring particle concentration in multiphase pipe flow using acoustic backscatter: Generalization of the dual-frequency inversion method, J. Acoust. Soc. Am., 136 (2014) 156-169.

[26] J. Bux, N. Paul, J.M. Dodds, J. Peakall, S. Biggs, T.N. Hunter, In situ characterization of mixing and sedimentation dynamics in an impinging jet ballast tank via acoustic backscatter, AIChE. J., 63 (2017) 2618-2629.

[27] J. Bux, J. Peakall, S. Biggs, T.N. Hunter, In situ characterisation of a concentrated colloidal titanium dioxide settling suspension and associated bed development: Application of an acoustic backscatter system, Powder Technol., 284 (2015) 530-540.

[28] T.N. Hunter, L. Darlison, J. Peakall, S. Biggs, Using a multi-frequency acoustic backscatter system as an in situ high concentration dispersion monitor, Chem. Eng. Sci., 80 (2012) 409-418.

[29] T.N. Hunter, J. Peakall, S. Biggs, An acoustic backscatter system for in situ concentration profiling of settling flocculated dispersions, Miner. Eng., 27–28 (2012) 20-27.

[30] T.N. Hunter, J. Peakall, S.R. Biggs, Ultrasonic velocimetry for the in situ characterisation of particulate settling and sedimentation, Miner. Eng., 24 (2011) 416-423.

[31] T.N. Hunter, J. Peakall, T.J. Unsworth, M.H. Acun, G. Keevil, H. Rice, S. Biggs, The influence of system scale on impinging jet sediment erosion: Observed using novel and standard measurement techniques, Chem. Eng. Res. Des., 91 (2013) 722-734.

[32] H.P. Rice, M. Fairweather, J. Peakall, T.N. Hunter, B. Mahmoud, S.R. Biggs, Particle concentration measurement and flow regime identification in multiphase pipe flow using a generalised dual-frequency inversion method, Procedia Eng., 102 (2015) 986-995.

[33] R.E. Challis, M.J.W. Povey, M.L. Mather, A.K. Holmes, Ultrasound techniques for characterizing colloidal dispersions, Rep. Prog. Phys., 68 (2005) 1541-1637.

[34] A.S. Dukhin, P.J. Goetz, C.W. Hamlet, Acoustic spectroscopy for concentrated polydisperse colloids with low density contrast, Langmuir, 12 (1996) 4998-5003.

[35] P.D. Thorne, C.E. Vincent, P.J. Hardcastle, S. Rehman, N. Pearson, Measuring suspended sediment concentrations using acoustic backscatter devices, Mar. Geol., 98 (1991) 7-16.

[36] P.D. Thorne, P.J. Hardcastle, R.L. Soulsby, Analysis of acoustic measurements of suspended sediments, J. Geophys. Res.-Oceans, 98 (1993) 899-910.

[37] B.D. Moate, P.D. Thorne, Interpreting acoustic backscatter from suspended sediments of different and mixed mineralogical composition, Cont. Shelf Res., 46 (2012) 67-82.

[38] P.D. Thorne, M.J. Buckingham, Measurements of scattering by suspensions of irregularly shaped sand particles and comparison with a single parameter modified sphere model, J. Acoust. Soc. Am., 116 (2004) 2876-2889.

[39] A.E. Hay, Sound scattering from a particle-laden, turbulent jet, The Journal of the Acoustical Society of America, 90 (1991) 2055-2074.

[40] K.F.E. Betteridge, P.D. Thorne, R.D. Cooke, Calibrating multi-frequency acoustic backscatter systems for studying near-bed suspended sediment transport processes, Cont. Shelf Res., 28 (2008) 227-235.

[41] R.J. Urick, The absorption of sound in suspensions of irregular particles, The Journal of the Acoustical Society of America, 20 (1948) 283-289.

[42] J. Bux, M.S. Manga, T.N. Hunter, S. Biggs, Manufacture of poly (methyl methacrylate) microspheres using membrane emulsification, Phil. Trans. R. Soc. A. 374:20150134, (2016).

[43] N.R. Brown, T.G. Leighton, S.D. Richards, A.D. Heathershaw, Measurement of viscous sound absorption at 50–150 kHz in a model turbid environment, J. Acoust. Soc. Am., 104 (1998) 2114-2120.

[44] P.D. Thorne, I.T. MacDonald, C.E. Vincent, Modelling acoustic scattering by suspended flocculating sediments, Cont. Shelf Res., 88 (2014) 81-91.

[45] C.E. Vincent, I.T. MacDonald, A flocculi model for the acoustic scattering from flocs, Cont. Shelf Res., 104 (2015) 15-24.

[46] C. Sahin, I. Safak, T.-J. Hsu, A. Sheremet, Observations of suspended sediment stratification from acoustic backscatter in muddy environments, Mar. Geol., 336 (2013) 24-32.

[47] H.P. Rice, M. Fairweather, J. Peakall, T.N. Hunter, B. Mahmoud, S.R. Biggs, Measurement of particle concentration in horizontal, multiphase pipe flow using acoustic methods: Limiting concentration and the effect of attenuation, Chemical Engineering Science, 126 (2015) 745-758.

[48] S. Temkin, Suspension Acoustics: An Introduction of the Physics of Suspensions, Cambridge University Press2005.

[49] D.M. Hanes, On the possibility of single-frequency acoustic measurement of sand and clay concentrations in uniform suspensions, Continental Shelf Research, 46 (2012) 64-66.

[50] C. Sahin, R. Verney, A. Sheremet, G. Voulgaris, Acoustic backscatter by suspended cohesive sediments: field observations, Seine Estuary, France, Cont. Shelf Res., 134 (2017) 39-51.

[51] G.W. Wilson, A.E. Hay, Acoustic backscatter inversion for suspended sediment concentration and size: A new approach using statistical inverse theory, Continental Shelf Research, 106 (2015) 130-139.

[52] F. Babick, A. Richter, Sound attenuation by small spheroidal particles due to visco-inertial coupling, J. Acoust. Soc. Am., 119 (2006) 1441-1448.

[53] S.D. Richards, T.G. Leighton, N.R. Brown, Visco–inertial absorption in dilute suspensions of irregular particles, Proceedings of the Royal Society of London. Series A: Mathematical, Physical and Engineering Sciences, 459 (2003).

Table 1: Material characteristics and corresponding experimental concentrations by weight and volume fraction.

Particle Type	d_{50} (μm)	ρ (kgm^{-3})	Shape	Experiment	M (kgm^{-3})	ϕ (vol%)	Dominant attenuation mechanism
Honite 16 (glass beads)	78.6	2470	sphere	$k_t{}^m$	0.3 - 7.9	0.01 - 0.3	Scattering
				$\zeta^m, k_s{}^m$	0.3 - 7.9	0.01 - 0.3	
Honite 22 (glass beads)	40.5	2453	sphere	$k_t{}^m$	0.1 – 9.4	0.004 –0.3	Scattering & viscous
				$\zeta^m, k_s{}^m$	0.1 - 75.9	0.004 - 3.0	
Barytes	7.9	4418	irregular jagged	$\zeta^m, k_s{}^m$	2.6 - 63.8	0.06 - 1.42	Viscous
Titania	7.2	3900	aggregated spheroid	$\zeta^m, k_s{}^m$	2.5 - 111.1	0.06 - 2.8	Viscous
pMMA[1] (latex beads)	2.3	1180	sphere	$\zeta^m, k_s{}^m$	3.0 - 87.9	0.25 – 7.3	Thermal
MMA[1] (droplets)	2.0	940	sphere	$\zeta^m, k_s{}^m$	14.8 - 113.1	1.6 – 12.0	Thermal

[1] Suspended in sodium dodecyl sulfate (SDS)-laced water to prevent coalescence.

Table 2: Sediment attenuation and backscattering constants for each sediment; as measured using the outlined method, ξ^m and $k_s{}^m$, and as predicted via the Betteridge et al. [40] heuristic expressions, $\xi_s{}^c$ and $k_s{}^c$.

Particle	f_r (MHz)	ξ^m (m^{2}kg^{-1})	$\xi_s{}^c$ (m^{2}kg^{-1})	$k_s{}^m$ (mkg$^{-1/2}$)	$k_s{}^c$ (mkg$^{-1/2}$)
Honite 16	1	0.047	0.002	0.110	0.099
(glass beads)	2	0.036	0.022	0.410	0.375
	4	0.247	0.213	1.340	1.190
	5	0.441	0.407	1.620	1.540
Honite 22	1	0.014	0.0003	0.040	0.037
(glass beads)	2	0.024	0.004	0.170	0.147
	4	0.096	0.048	0.650	0.554
	5	0.181	0.103	0.990	0.828
Barytes[1]	1	0.115	-	0.020	-
	2	0.189	-	0.060	-
Titania[2]	2	0.238	-	0.117	-
	4	0.400	-	0.300	-
pMMA	1	0.095	-	0.023	-
Latex	2	0.125	-	0.032	-
(beads)	4	0.136	-	0.046	-
MMA	1	0.060	-	-	-
Emulsion	2	0.062	-	-	-
(droplets)	4	0.069	-	-	-

[1] Data source; Bux et al. [26]

[2] Data source; Bux et al. [27]

Table 3: Comparison of transducer constants; measured k_t^m, and k_t^c calculated from Betteridge, Thorne and Cooke [40] heuristic equations, for χ and f, and corresponding standard deviations.

Set	Frequency (MHz)	Average k_t^m			Average k_t^c		
1	1	0.0322	±	0.0030	0.0244	±	0.0045
	2	0.0076	±	0.0010	0.0086	±	0.0006
	4	0.0012	±	0.0002	0.0013	±	0.0001
2	1	0.0259	±	0.0024	0.0288	±	0.0097
	2	0.0077	±	0.0010	0.0088	±	0.0006
	4	0.0084	±	0.0016	0.0093	±	0.0004
	5	0.0067	±	0.0012	0.0072	±	0.0004
3	1	0.0267	±	0.0025	0.0228	±	0.0000
	2	0.0082	±	0.0012	0.0092	±	0.0004

Table 4: Comparison of the measured form factor values (f^m, derived from the measured scattering constants k^s_m) for pMMA and barytes, with values calculated from the Thorne and Meral scattering model, corrected for polydispersity (f^c) [24], as described in Eq. A.10 within the Appendix.

Particle type	Frequency (MHz)	Measured form factor, f^m	Corrected estimated form factor, f^c
pMMA	1	8.1×10^{-4}	6.3×10^{-5}
	2	1.2×10^{-3}	2.5×10^{-4}
	4	1.7×10^{-3}	1.0×10^{-3}
Barytes	1	1.7×10^{-3}	1.6×10^{-3}
	2	4.0×10^{-3}	6.1×10^{-3}
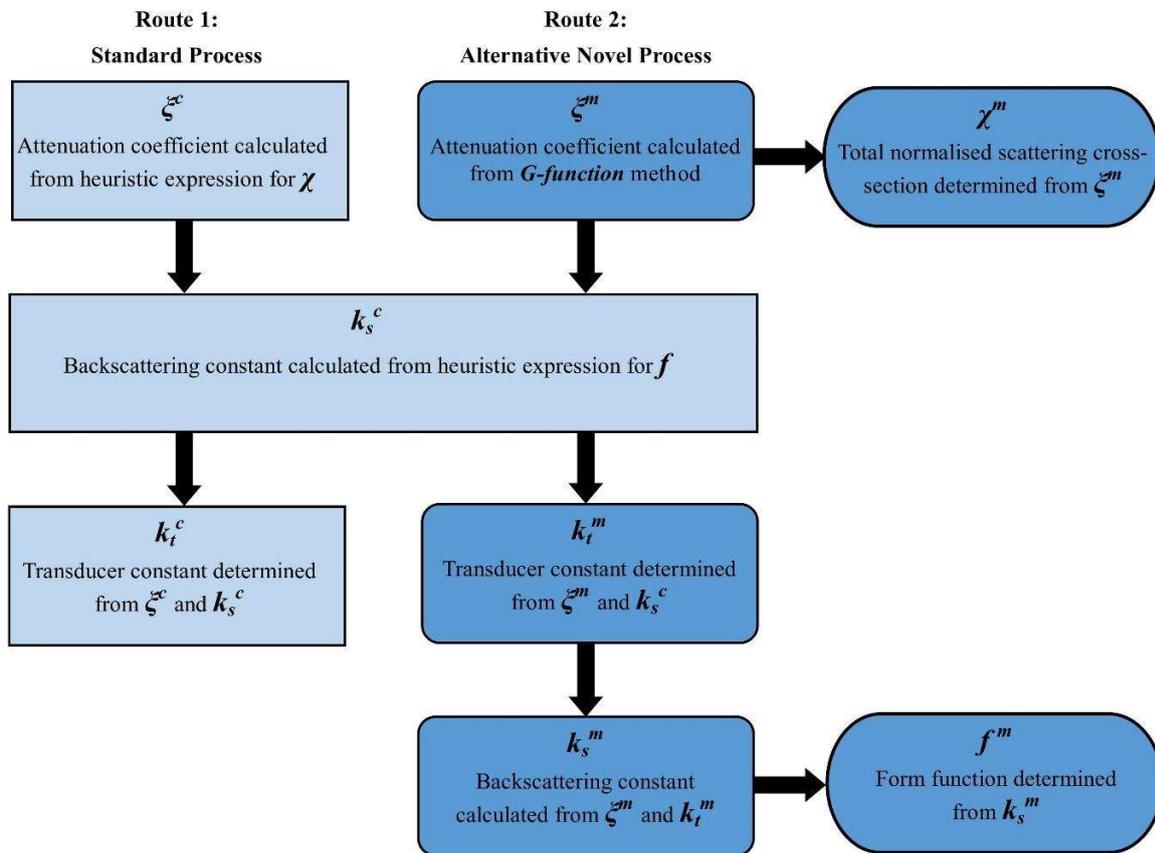
Figure 1: Flowchart illustrating two routes for determining acoustic constants; Route 1 requires heuristic expressions given in Appendix (Eqs. A.6-A.9). Route 2 combines direct measurement of the attenuation constant with heuristic expressions for calibration.
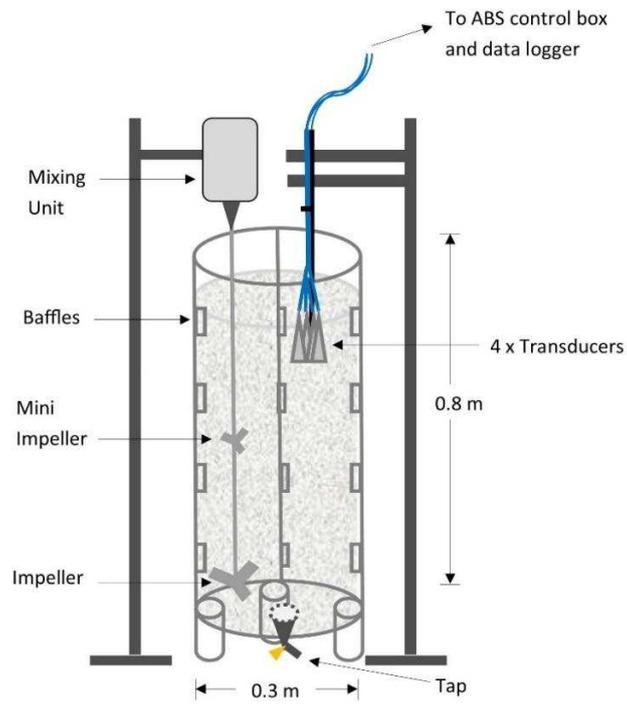
Figure 2: Schematic of calibration mixing tank.
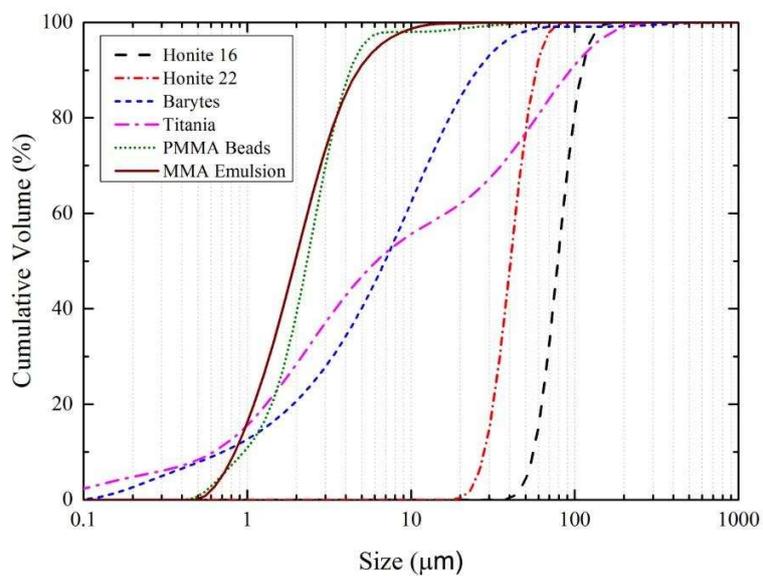
Figure 3: Cumulative size distributions of all particle systems.
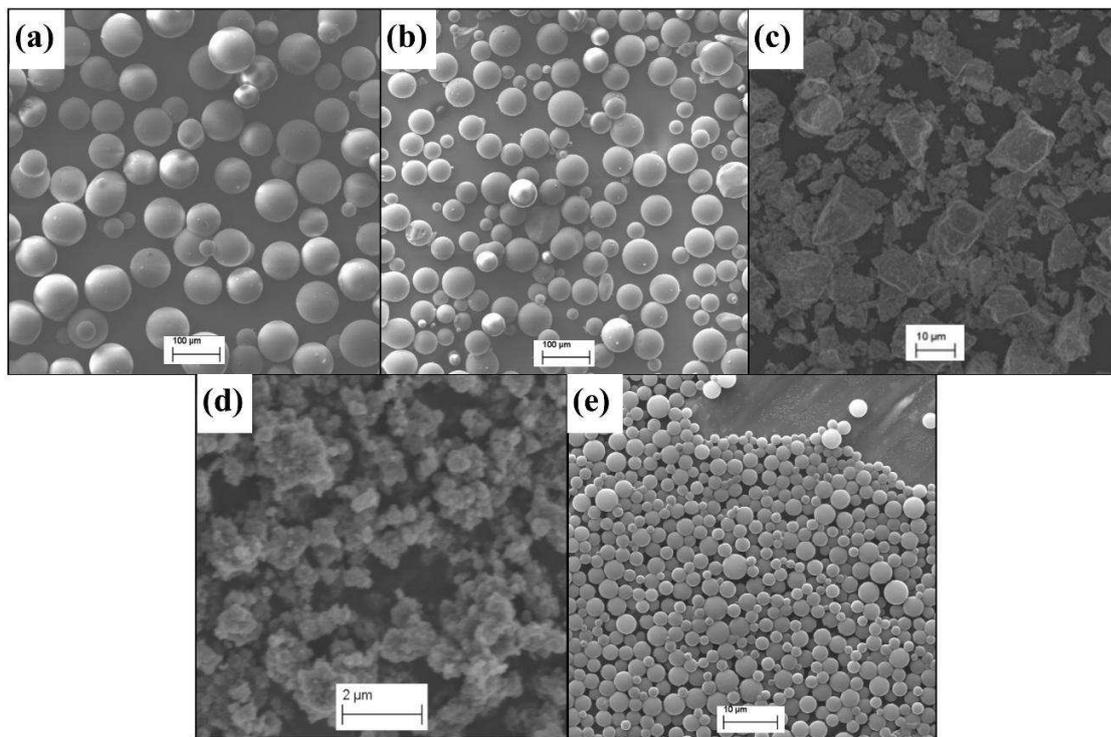
Figure 4: SEM images of all particle systems (at x magnification); (a) Honite 16 glass beads (x263), (b) Honite 22 glass beads (x348), (c) Barytes (x3k), (d) Titania (x4k), and (e) pMMA latex beads (x3k).
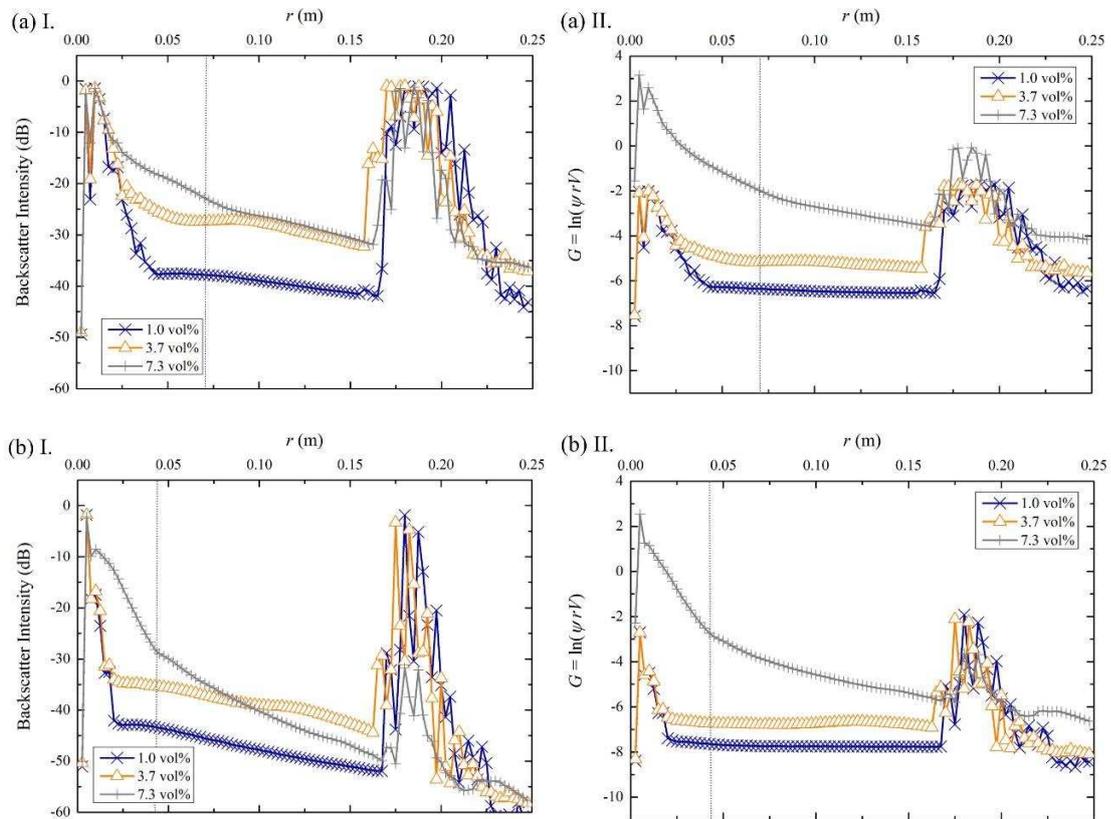
Figure 5: I. Backscatter intensity versus distance from transducer, and II. G-function versus distance from transducer of pMMA latex bead suspensions at three volume fractions at (a) 1 MHz and (b) 2 MHz frequencies, boundaries between near and far fields given by vertical dotted lines.
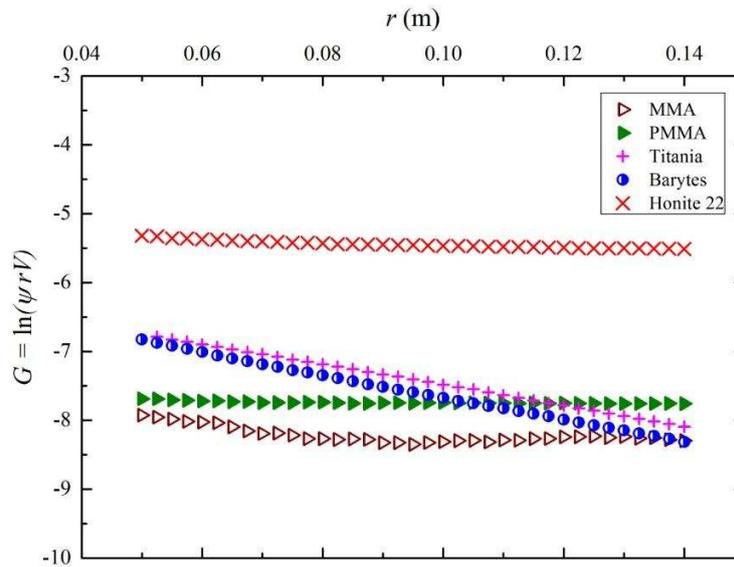
Figure 6: G-function versus distance from 2 MHz transducers, for MMA emulsions and corresponding pMMA beads, titania, barytes and Honite 22 (smaller glass) dispersions at 1 vol%. Backscatter data for titania taken from [27] and for barytes from [26]. Data for Honite 22 given in Supplementary Materials, Figs. S1-S2.
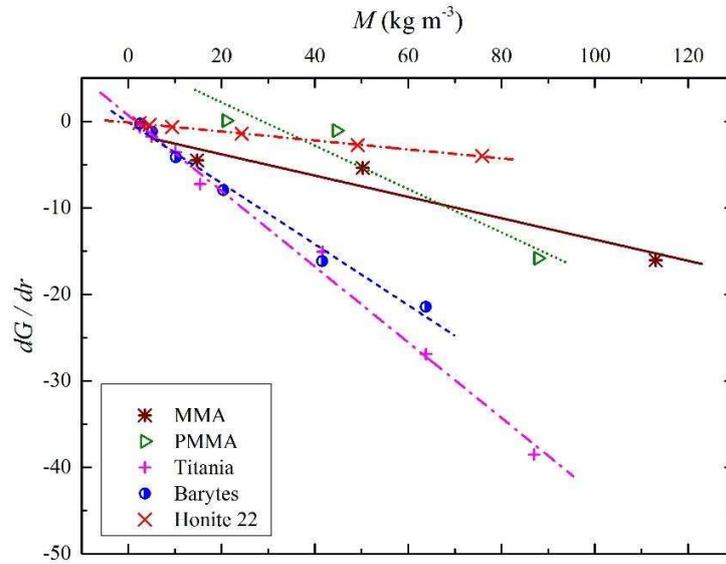
Figure 7: dG/dr versus nominal concentration M, for MMA, pMMA, titania, barytes and Honite 22 at 2 MHz.
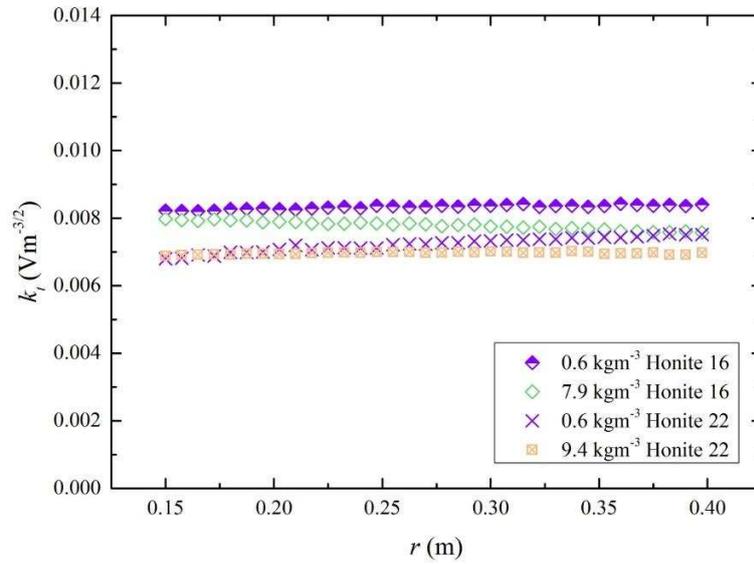
Figure 8: Measured transducer constant, k_t^m, with respect to transducer range r, determined from measured ζ^m and k_s^m derived from the Betteridge et al. [40] heuristic expression, for Honite 16 (larger glass) and Honite 22 (smaller glass). Comparison of data obtained via a 2 MHz probe at two concentrations.
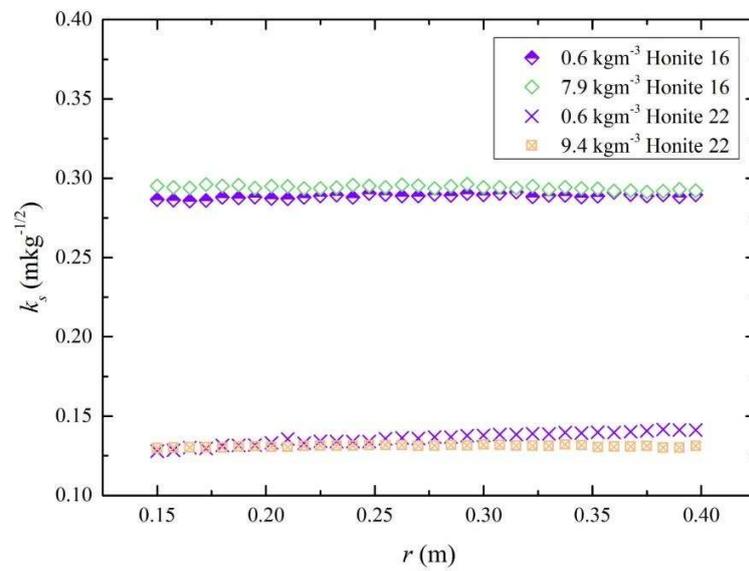
Figure 9: Measured backscattering constant, k_s^m, with respect to transducer range r, derived from ζ^m and k_t^m for Honite 16 and Honite 22. Comparison of data obtained via a 2 MHz probe, at two concentrations.
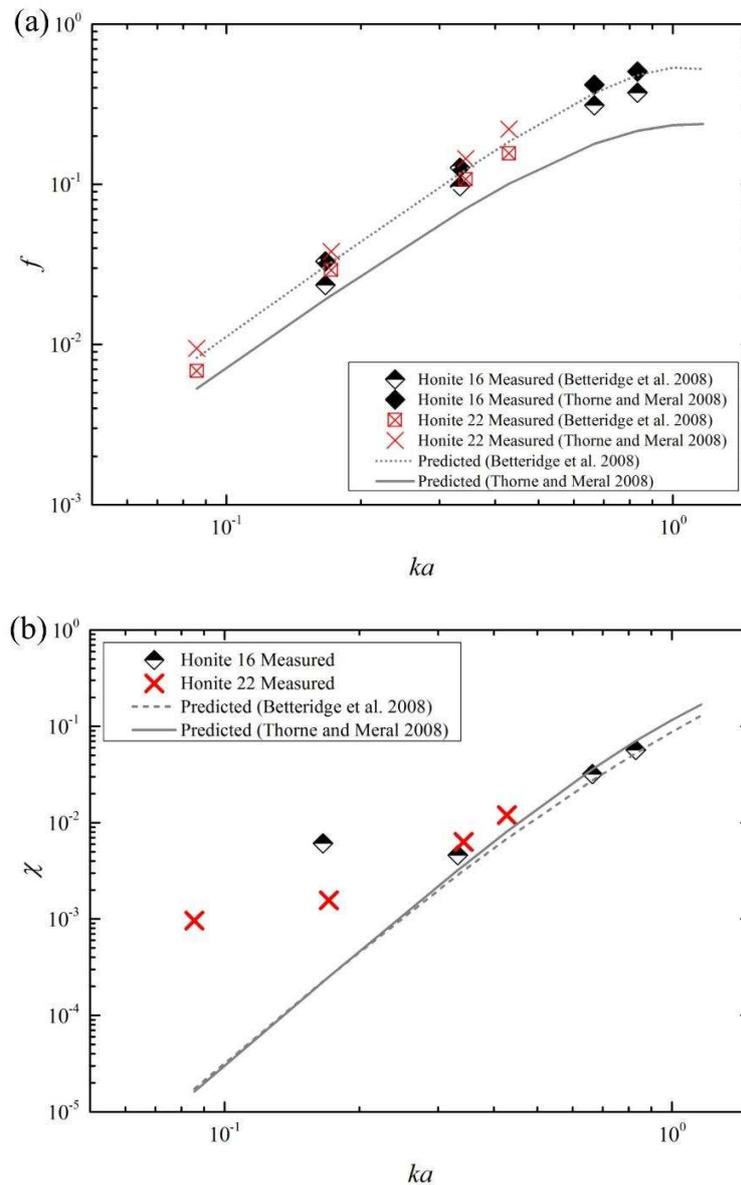
Figure 10: (a) Form function f versus ka and (b) total normalized scattering cross-section χ versus ka, for Honite 16 (larger glass) and Honite 22 (smaller glass). Data points represent parameters derived from the G-function analysis method (Route 2), and are compared with predictions (Route 1) utilising expressions for spherical glass particles (Betteridge et al. 2008 [40]) and sandy sediments (Thorne and Meral 2008 [24]). Routes are defined in Fig. 1.
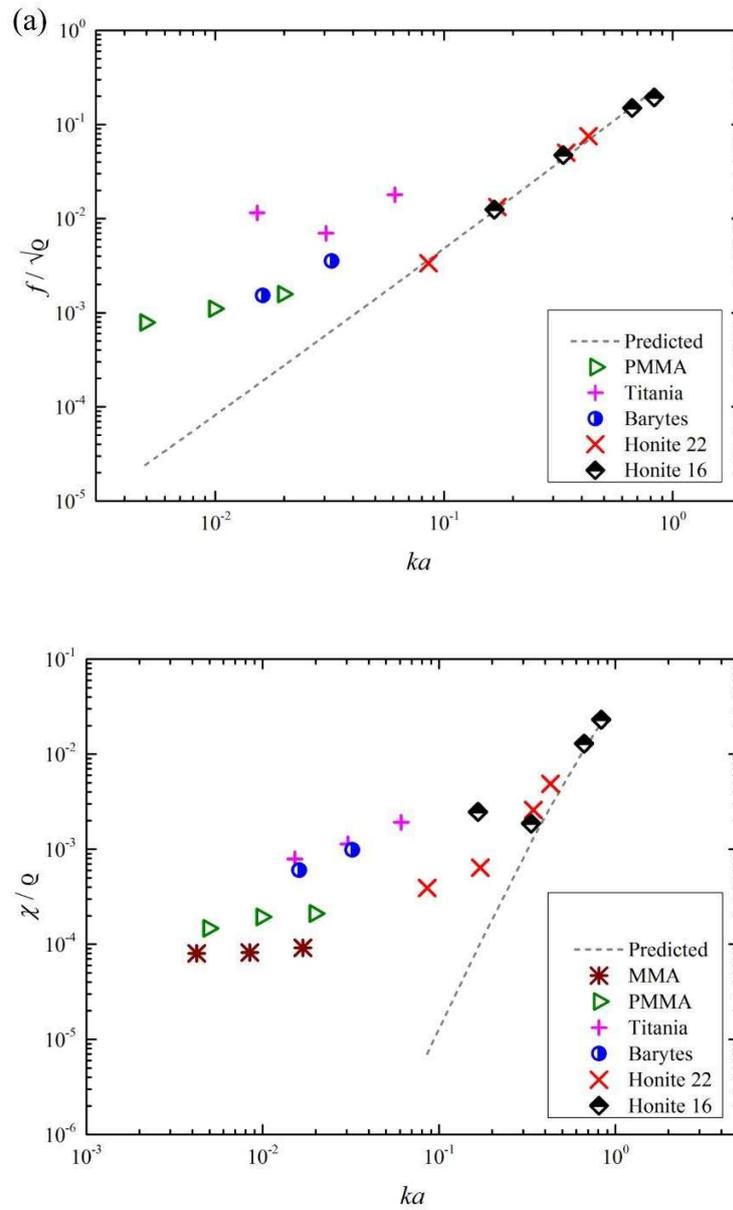
Figure 11: (a) Form function normalised by square-root of specific gravity, and (b) total scattering cross-section normalised by specific gravity. Predictions made via Betteridge et al. [40] expressions subsequently normalised in the same way.
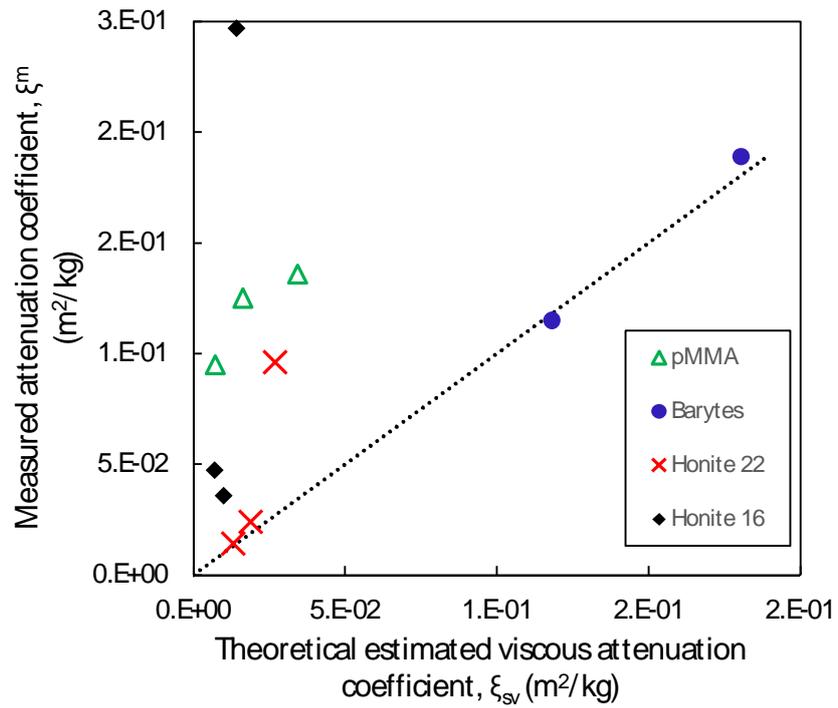
Figure 12: Measured attenuation coefficients (ξ^m) versus theoretical estimations of viscous absorption (ξ^c_{sv}) calculated using Eqs. 5-8, for pMMA, barytes, Honite 22 and Honite 16. Dotted line reflects 1:1 relationship.